

# Configurable Electronics with Low Noise and 14-bit Dynamic Range for Photodiode-based Photon Detectors

Hans Muller<sup>1</sup>, Rui Pimenta<sup>1</sup>, Zhongbao Yin<sup>2</sup>, Daicui Zhou<sup>2</sup>, Xi Cao<sup>3</sup>, Qingxia Li<sup>3</sup>, Yingzhuang Liu<sup>3</sup>, FeiFei Zou<sup>3</sup>, Bernhard Skaali<sup>4</sup>, and Terry C. Awes<sup>5</sup>

<sup>1</sup> CERN, PH department, 1211 Geneva 23, Switzerland, <sup>2</sup> Institute of Particle Physics, Huazhong Normal University, Wuhan 43007, China, <sup>3</sup> Electronics and Information Department, Huazhong University of Science and Technology, Wuhan 430074, China, <sup>4</sup> Department of Physics, University of Oslo, Blindern 0316, Norway, <sup>5</sup> Oak Ridge National Laboratory, Oak Ridge, TN 37831, USA

We describe the principles and measured performance characteristics of custom designed configurable 32-channel shaper/digitizer front-end electronics (FEE) cards with 14-bit dynamic range for use with gain-adjustable photon detectors. The electronics has been designed for the PHOS calorimeter of ALICE with avalanche photodiode (APD) readout operated at -25 C ambient temperature and a signal shaping time of 1  $\mu$ s. The electronics has also been adopted by the EMCal detector of ALICE with the same APD readout, but operated at an ambient temperature of +25 C and with a shaping time of 100ns. The CR-RC2 signal shapers on the FEE cards are implemented in discrete logic on a 10-layer board with two shaper sections for each input channel. The two shaper sections are implemented with a gain ratio of 1:16 and digitized with 10-bit ADCs to provide an effective dynamic range of 14 bits. Gain adjustment in the range of 240-400V for each individual detector APD is available through 32 bias voltage control registers of 10-bit range. The fixed gains and shaping times of the pole-zero compensated shapers are defined prior to FEE production according to choice of a few R and C components. For trigger purposes, “fast-OR” outputs with 12-bit dynamic range are available. FPGA-based slave logic, combined with a USB processor supports a variety of remote control and monitoring features, including APD gain calibration. The measurements presented here for APDs at -25 C ambient temperature and 1  $\mu$ s shaping time achieve an average RMS noise level of 0.26 ADC counts or 290 electrons. The linearity over the dynamic range is better than 1% as is the uniformity of shaping time and gain over 32 channels. Due to the excellent correspondence of the output pulse shape with offline fits, a differential timing resolution of less than 1.5 ns between channels has been achieved at ca 2GeV, i.e. at 1.5% of the dynamic range of PHOS.

## Photoelectron signal

The PHOS detector [1] of ALICE is an electromagnetic calorimeter consisting of 17920 PWO<sub>4</sub> crystals. The detector is operated at an ambient temperature of -25C to enhance the scintillation light yield. Each crystal is read out by an Avalanche Photo-Diode (APD) of type S8148, produced by Hamamatsu Co, Japan. These APDs have an active area of 0.5×0.5 cm<sup>2</sup> and are mounted in a ceramic case of 0.9×1.1 cm<sup>2</sup>. The EMCal detector [19] of ALICE is a large area lead/scintillator sampling calorimeter with “shashlik”-type readout via wavelength shifting fibers and consists of 12672 readout towers. The fiber bundle of each tower is read out with a S8148 APD operated at ambient temperature of the ALICE experiment (+25C). Tests of the FEE electronics described here have been performed with S8148 APDs excited with photon pulses which imitate the characteristics of PWO<sub>4</sub> scintillation light via LEDs of type Kingbright L7104PCB with 470 nm peak wavelength.

The number of photoelectrons produced by an APD from the scintillating light of a 1MeV electromagnetic particle in a PWO<sub>4</sub> crystal at temperature +25°C for a gain M=1 can be estimated from PWO<sub>4</sub> light yield measurements [1]. By using an EMI 9814b PMT photomultiplier which covers the full exit window and by putting detector surfaces and quantum efficiencies of PMT and APD in relation for a nominal PWO<sub>4</sub> light-yield of 10 at +25 °C one obtains:

$$N_{APD} = N_{PMT} \times (S_{APD}/S_{PMT}) \times (E_{APD}/E_{PMT}) = 10 \times (25/484) \times (0.7/0.25) = \underline{1.45e/MeV}$$

At the PHOS operating temperature of -25 C the light-yield is ca. 3 times higher, hence

$$N_{APD(-25C, M=1)} \sim 4.4 e/MeV$$

With a nominal APD gain for PHOS of M=50, the APD charge signal is:

$$N_{APD(-25C, M=50)} \sim 220 e/MeV$$

Light-yield estimates from cosmic ray muon measurements for the EMCal gave corresponding numbers for the EMCal of

$$N_{\text{APD}(25\text{C},M=1)}^{\text{EMC}} \sim 2.5 \text{ e/MeV} \text{ and } N_{\text{APD}(25\text{C},M=50)}^{\text{EMC}} \sim 125 \text{ e/MeV}$$

With a 1.2pF charge capacitor of the preamplifier, the charge conversion gain is 0.83 V/pC and the preamplifier output step voltage for PHOS and EMCal at APD gain  $M=50$  are:

$$U_{\text{step}(-25\text{C},M=50)} \sim 29.2 \text{ } \mu\text{V/MeV} \text{ and } U_{\text{step}(M=50)}^{\text{EMC}} \sim 16.6 \text{ } \mu\text{V/MeV}$$

respectively.

## Dynamic range

The dynamic range has been defined by the requirement of 80 GeV maximum single channel energy for PHOS and 250 GeV maximum single channel energy for EMCal. Given the  $16:1=2^4$  gain ratio of the high and low gain channels, the two overlapping 10-bit ADC ranges correspond to an effective 14-bit dynamic range.

High gain: 4.9 MeV to 5 GeV (PHOS) and 15.3 MeV to 15.6 GeV (EMCal)

Low gain: 78 MeV to 80 GeV (PHOS) and 248 MeV to 250 GeV (EMCal)

The minimum value corresponds to the least significant bit of the 10-bit ADC. The digital resolution is the resolution given by the least significant bit value relative to a signal of energy  $E$ . For the above PHOS ranges, the digital resolutions  $\Delta E/E=4.9/E$  [MeV] for high gain and  $\Delta E/E=78/E$  [MeV] for low gain are shown in Fig. 1, together with first testbeam data taken by PHOS with old electronics [2]. Apart from a small region above 5 GeV, the digital resolution lies always significantly below the targeted PHOS energy resolution of  $\sim 3\%/\text{SQRT}(E)$ .

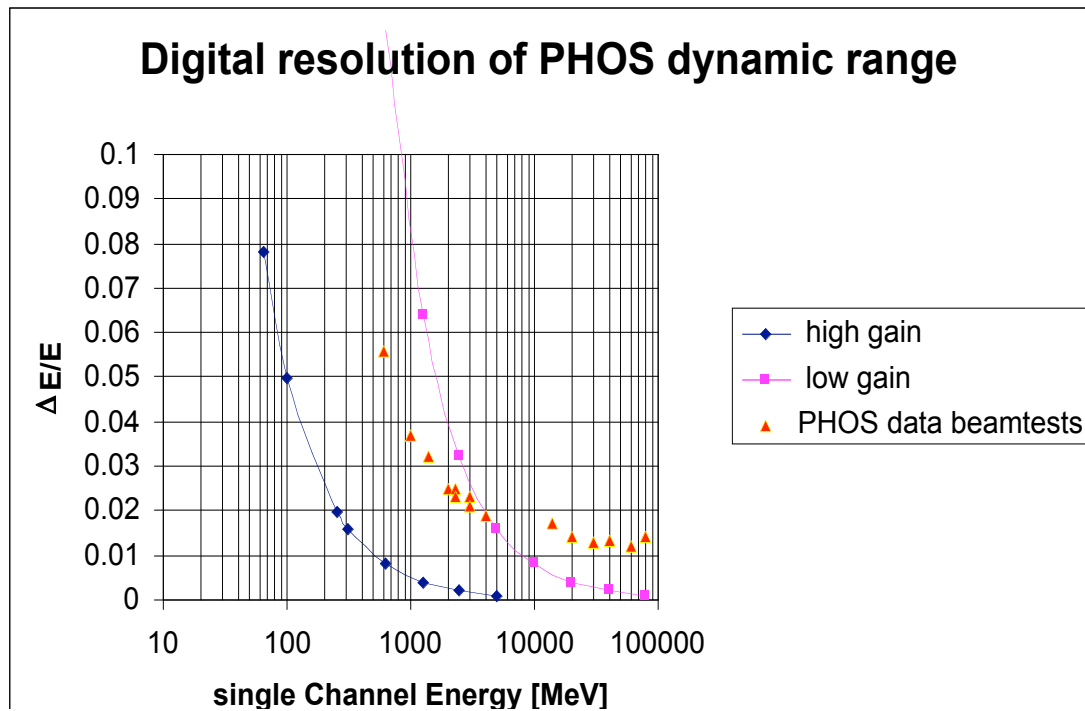


Fig. 1. Digital resolution over PHOS dynamic range.

The intrinsic energy resolution of the EMCal is expected from simulations to be about  $8.5\%/\text{SQRT}(E)$ . The relative contribution of the digital resolution to the total EMCal resolution is shown in Fig. 2. A 1% constant resolution contribution due to tower inter-calibration error is assumed.

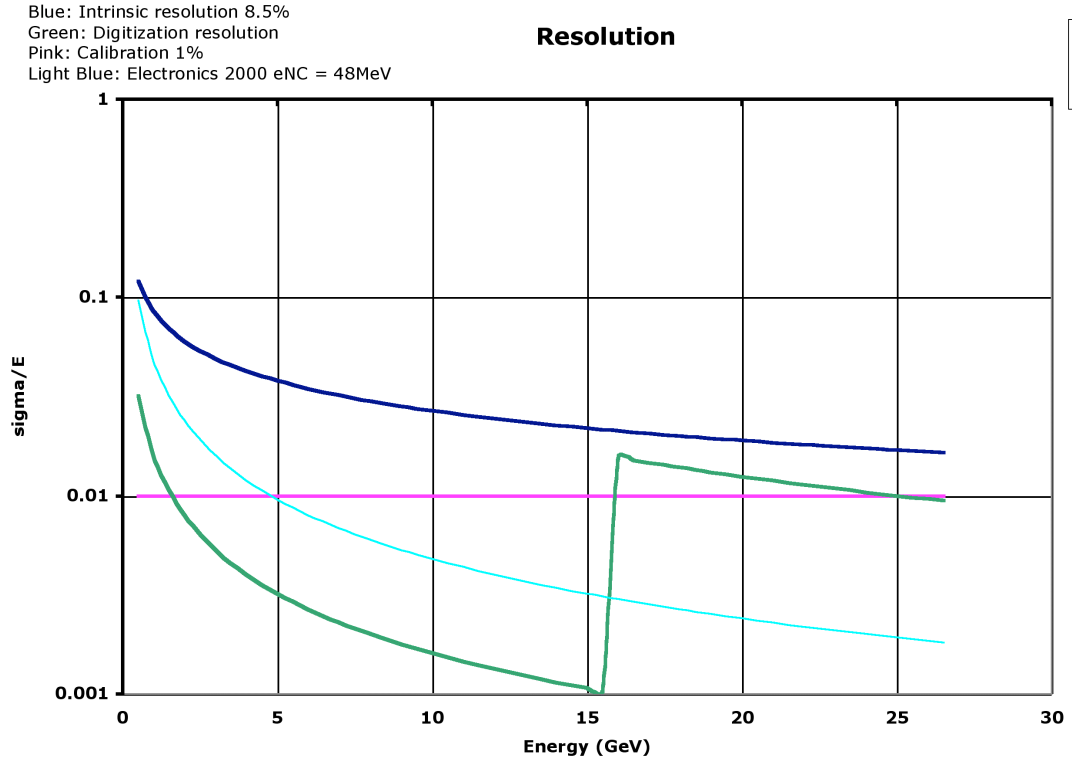


Fig. 2. Various contributions to the EMCal energy resolution.

The shaper gain is defined with the above choices since the maximum energies must correspond to the maximum analogue input ADC Voltage of 1.0 Volt. In the case of PHOS with the above nominal preamplifier output of 29.2 $\mu$ V/MeV the two gain ranges are defined as:

High gain: LSB= 143  $\mu$ V (5.0 MeV), Umax= 0.146 Volt (5 GeV) -> **shaper gain = 6.85**

Low gain: LSB= 2.28 mV(78 MeV), Umax= 2.34 Volt (80 GeV) -> **shaper gain = 0.427**

And in the case of EMCal with the above nominal preamplifier output of 16.6 $\mu$ V/MeV the two gain ranges are defined as:

High gain: LSB= 254  $\mu$ V (15.3 MeV), Umax= 0.259 Volt (15.6 GeV) -> **shaper gain = 3.89**

Low gain: LSB= 4.11 mV(248 MeV), Umax= 4.15 Volt (250 GeV) -> **shaper gain = 0.24**

The actual implementation does not need to reproduce these exact gain values since the assumptions about light-yield are only nominal and may be adjusted via the APD gains.

## Energy resolution

The energy resolution of the calorimeter is parameterized as [1]

$$\frac{\sigma}{E} = \sqrt{\frac{a^2}{E^2} + \frac{b^2}{E} + c^2}$$

with the following parameters:

- noise term a: parallel and serial noise from detector diode and preamplifier
- stochastic term b: shower fluctuations and APD excess noise
- constant term c: detection losses, inter-calibration of channels, non-uniformity, non-linearity, instabilities (temperature and bias)

In the case of PHOS, a fit to PHOS test beam data [2], gives the following preliminary values:  $a=13$  MeV ( $3 \times 3$  crystals),  $b=3.58\%$   $\text{GeV}^{0.5}$ ,  $c=1.12\%$ . For the high energy region  $E > 1$  GeV, the fit parameters are compatible with

$$\frac{\sigma}{E} = \frac{3\%}{\sqrt{E}} \oplus 0.8\%$$

The interest in a high signal/noise ratio is to achieve a low energy resolution at low energies around the two photon invariant mass peaks of the  $\pi^0$  (134.97 MeV) and  $\eta$  (547.75 MeV) for accurate measurements and energy calibration of the calorimeter [3].

## Channel readout

Fig.3 depicts the readout principles for one FEE channel. An APD is biased via a resistor  $R_p$  to a voltage which corresponds to the required avalanche gain. The charge produced by the photodiode is the product of number of photoelectrons and APD gain. As noted above, with gain  $M=50$  the nominal detector charge is  $Q=220$  e/MeV for PHOS ( $Q=125$  e/MeV EMCal). For further signal analysis, the charge dynamics is approximated as a delta function, although in reality, the scintillating light of the  $\text{PWO}_4$  crystals has a finite rise- and decay-time (of order 1ns and 10 ns, respectively). Ideally, the charge sensitive amplifier (CSA) converts the delta charge into a voltage step of amplitude  $U=Q/C_f$ . In reality the step function has a finite risetime of order 20 ns which is also limited by the finite rise-time of the CSA. For simplicity, the capacitor is auto-discharged via a resistor  $R_{dis}$  with a time-constant that is very large (of order 100  $\mu\text{s}$ ) compared to the time of measurement. The CSA and photodiode are physically close to the calorimeter, hence operated at the detector's ambient temperature.

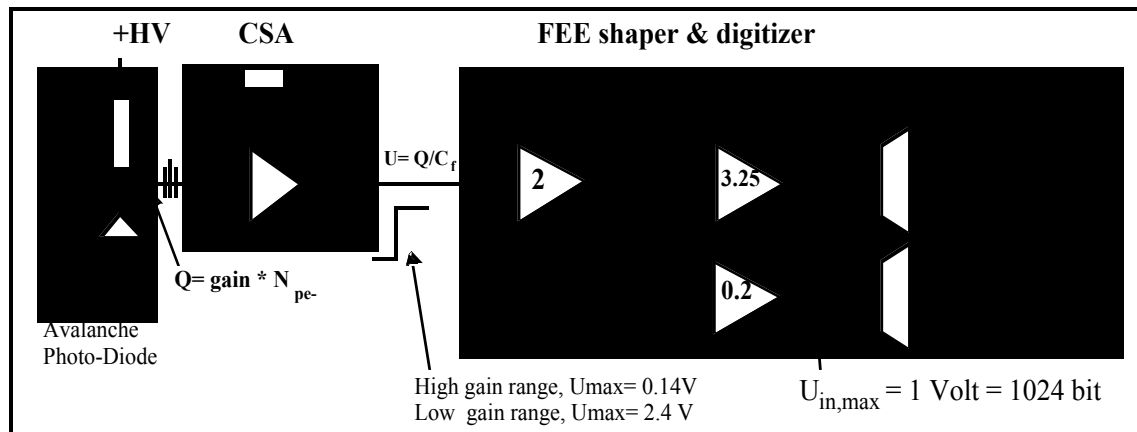


Fig. 3. Photodiode and preamplifier, followed by dual gain shaper and ADC's.

The CSA step signal is connected via a short length cable to the shaper and digitizer of the FEE electronics where it is amplified by a low noise buffer, followed by two parallel CR-RC2 shapers of equal time constant and gain ratio of 16:1. The products of the buffer gain and the shaper gains correspond to the gains required for the given dynamic range. For each shaper section of high and low gain, there is one 10-bit ADC to digitize the data.

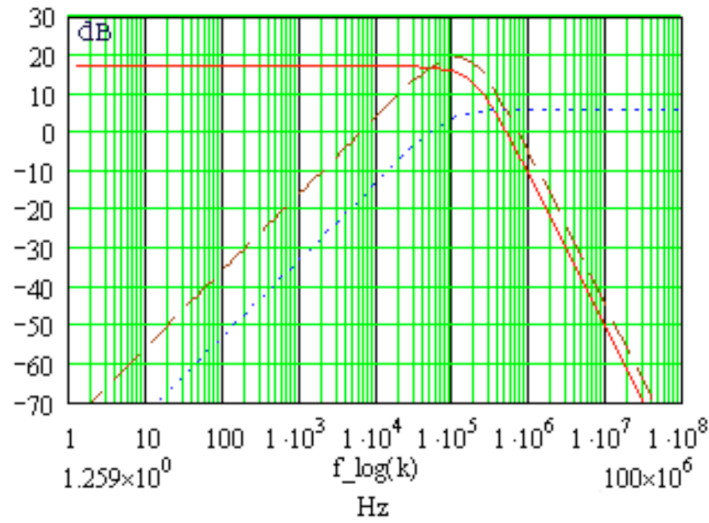
## Shaper bandpass

The shaper implemented in the PHOS FEE electronics is a second-order bandpass filter for a central frequency  $f_c = 1/(2\pi * \tau)$  where  $\tau$  is the shaping constant. It consists of a high-pass, followed by two low-pass filters with a -3dB cutoff frequency  $f_c$ . The purpose of the shaper bandpass is to enhance the Signal-over-Noise ratio by separating the noise spectrum from the signal's main Fourier components.

The noise components are:

- Current noise (parallel): Shottky  $2qI_d$  + shunt resistor thermal current  $4kT/R_b$  + equivalent input current (proportional shaping time)

- Voltage noise (serial)  $4kTR_s$  thermal Johnson noise at the amplifier input (inversely proportional shaping time)
- $1/f$  noise (independent of shaping time)



Magnitude Response of Shaper, HPF, LPF

Fig. 4. Bode diagram of the PHOS shaper bandpass for  $\tau=1\mu s$ .

The Bode diagram of Fig. 4 depicts the high (dotted) and low (solid red) bandpass characteristics as well as the combined bandpass transfer curve (interrupted line). The peak frequency  $f_c = 160$  kHz) corresponds with  $f_c = 1/(2\pi\tau)$  to the shaping time of  $\tau=1\mu s$ .

## Signal over noise

With the aim to achieve a low energy resolution also at low energies, a shaper was designed with a low-noise input buffer stage. The noise of cascaded amplifiers with  $N1$  and  $N2$  noise levels is calculated as

$K1$  is the amplification of the first buffer stage. By choosing  $K1 > 1$  the contribution of the shaper noise  $N2$  can be reduced by choosing a buffer with a low-noise figure  $N1$ .

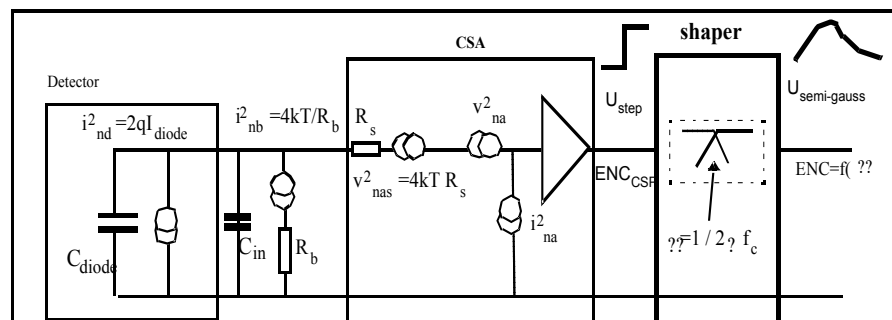


Fig. 5. Equivalent diagram of detector and preamplifier, followed by the shaper bandpass.

The standard noise analysis [4] is depicted in Fig 5. The equivalent noise charge ENC at the output of the shaper is a function of the shaping time constant  $\tau$ , of absolute temperature  $T$ , of the parallel, serial, and constant noise sources and of the detector capacitance. The current noise is proportional to shaping time  $\tau$ , the voltage noise is inversely proportional to  $\tau$ , and the  $1/f$  noise is independent of  $\tau$ . With an estimate for  $R_s = 2/3 * (1/g_m)$  where  $g_m$  is the forward trans-conductance of the JFET transistor, the ENC as function of shaping time is given by:

$$ENC^2 = \frac{4kT}{q^2 R_p} F + \frac{4kT}{q^2} F_s^2 \frac{1}{g_m} \frac{C_d^2}{\tau} + C_d^2 \tau \text{const}$$

For the PHOS electronics,  $R_p = 20 \text{ MOhm}$ ,  $g_m = 30 \text{ mS}$ , and  $C_d = 100 \text{ pF}$  (APD= 90pF @ -25 C, JFET=10 pF). The noise figures [5] for a CR-RC2 shaper are  $F_s=0.84$  and  $F_p = 0.63$ .

The corresponding ENC noise (without the negligible constant  $1/f$  noise term) in dependence on shaping time  $\tau$  is shown in Fig 6. The minimum noise is achieved at 2...3  $\mu\text{s}$ . At shorter shaping times the serial noise dominates, while at higher shaping times the current noise dominates.

PHOS has nevertheless chosen a time constant of  $1\mu\text{s}$  as a compromise for improved offline timing resolution (see chap. “Comparative Measurement with  $2\mu\text{s}$  shaping time”). The measured average RMS noise level of 0.26 ADC counts (see chapter “Pedestals and RMS”) for  $\tau=1$  corresponds to  $39\mu\text{V}$  at the output of the preamplifier, or with  $N_{q\text{noise}}=1/q (U \times C_f)$  this corresponds to 292 noise electrons.

In the case of the EMCal, the intrinsic resolution is worse than PHOS and so the electronics noise contribution is less important. As shown in Fig.2, an electronics noise contribution of as much as 2000 electrons is not significant relative to the intrinsic resolution. Therefore EMCal has chosen a much shorter shaping time of 100 ns to suppress contributions to the signal from energy deposit by late event-related neutron background, and to reduce the data volume per channel.

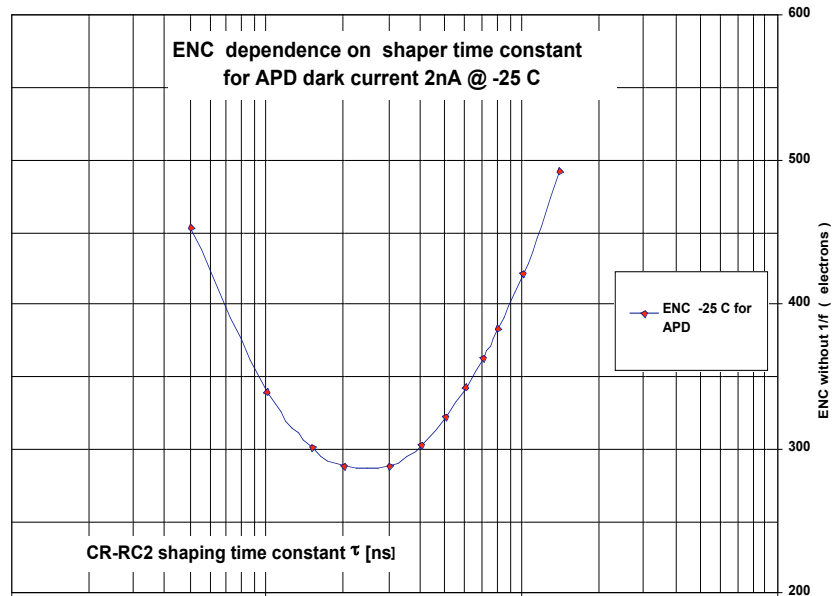


Fig. 6. Noise as function of shaping time for PHOS APD at -25 C.

## Shaper analysis

The Laplace representation of n-th order CR-RCn shapers with step function input from a charge sensitive amplifier is derived as the product of equivalent operators, including the preamplifier. With a Laplace equivalent  $s$  for the step Voltage,

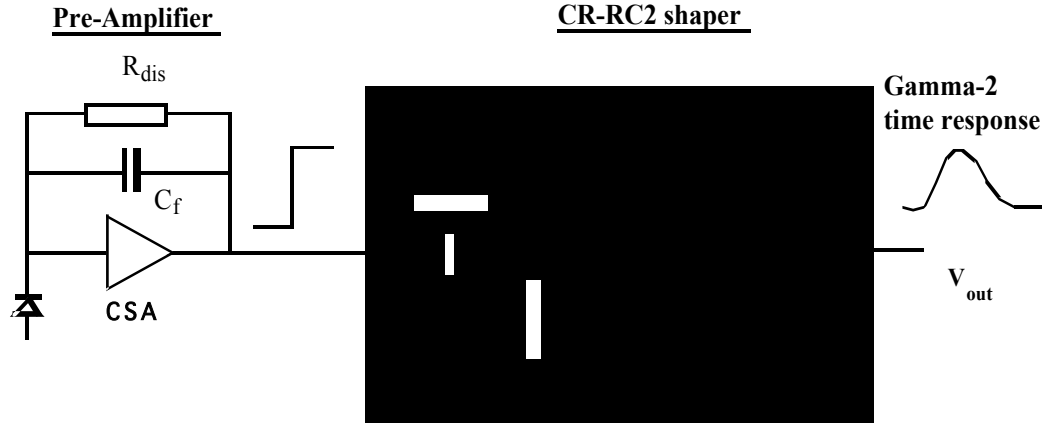


Fig. 7. Full analogue electronic stages diagram of CR-2RC shaper.

Fig.7 can be transcribed with shaping constant  $\tau_0$  and shaper gain A into the following Laplace operator, representing the full chain of the FEE electronics analogue part:

$$H_{CSA\text{shaper}} = s \left[ \frac{1}{1 + \frac{1}{R_{dis} C_f}} \right] \left[ \frac{\tau_0}{1 + s\tau_0} \right] \left[ \frac{A}{1 + s\tau_0} \right]^n$$

The first bracket term is the pole-zero cancellation term for the auto-discharge combination  $R_{dis} * C$  of the CSA. As shown below, this term can be cancelled by including the inverse operator as “pole-zero-cancellation” RC network in the input of the shaper. The second bracket is the  $C_p * R_d$  differentiator and the third term are n integrator stages. The shaping time constants  $\tau_0$  of differentiator and integrators are chosen equal. The general solution [5] of this Laplace operator in the time domain is a Gamma function of order n:

$$V_n(t) = \left[ \frac{n! Q A^n}{C_f n!} \right] \left[ \frac{t}{\tau_0} \right]^n e^{-\frac{t}{\tau_0}}$$

The zero-crossing of the first derivate shows that the peak amplitude is proportional to the observable  $Q \sim E$ .

$$V_{max} = \frac{Q A^n}{C_f n!} e^{-1}$$

For the n=2 second-order shaper, the output shape in the time domain is described with a peaking time  $\tau_p$  at  $V_{max}$ . The relation between peaking time and shaping time is  $\tau_p = n * \tau_0$ , hence for FEE electronics with n=2:

**peaking time = 2 \* shaping time**

$$V_{out}(t) = \left[ \frac{2 Q A^2}{C_f} \right] \left[ \frac{t - \tau_0}{\tau_0} \right]^2 e^{-\frac{t - \tau_0}{\tau_0}}$$

## Shaper implementation

The differentiator stage can simply be implemented as  $R_0 * C_z = 1/(2\pi f_c)$  combination at the input of the low noise buffer in front of the integrators (Fig. 8). In order to cancel the pole-zero operator of the full Laplace description of the full chain, it is sufficient to add a resistor  $R_z$  in parallel to  $C_z$  and choose the combined time constant equal to  $R_{dis} * C_f$ . In the real application, the value of  $R_z$  is determined by measurement.

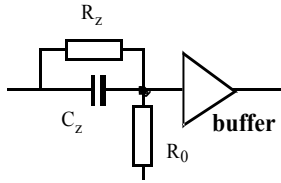


Fig.8. Differentiator and pole-zero cancellation stage of the shaper.

The combined resistor vales of the differentiation and pole-zero cancellation are listed in Table 1 for two shaping times.

shaper constant $\tau_0$	$R_z$	$C_z$	$R_o$
$\tau_0=2\mu s$	143 k	470 pF	9.1 k
$\tau_0=1\mu s$	143 k	470 pF	4.22 k

Table 1. Values of differentiator and pole-zero filter for 1 and 2  $\mu s$  shaping time.

The effect of the CSA auto-discharge term can be seen in Fig 9 by replacing the CSA with a step pulse generator. The pole-zero cancellation filter produces an undershoot which would normally compensate the signal overshoot due to the CSA (first Laplace term). The fully compensated FEE pulse with CSA is shown later in Fig 12.

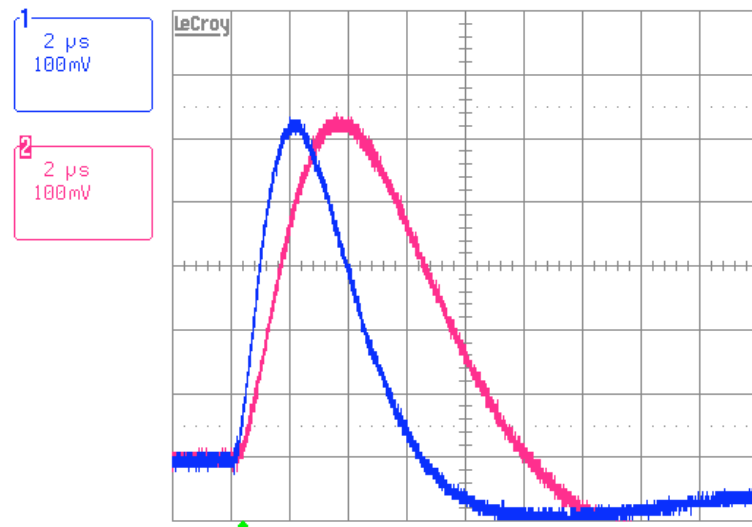


Fig. 9. Oscilloscope output of uncompensated step pulser response for two shaping times: 1  $\mu s$  and 2  $\mu s$ .

The double integrator stage has been implemented using a single operational amplifier with multiple feedback architecture (MFB) as shown in Fig. 10. The values of the components are obtained as solution of the transfer equations, described in the following sections:



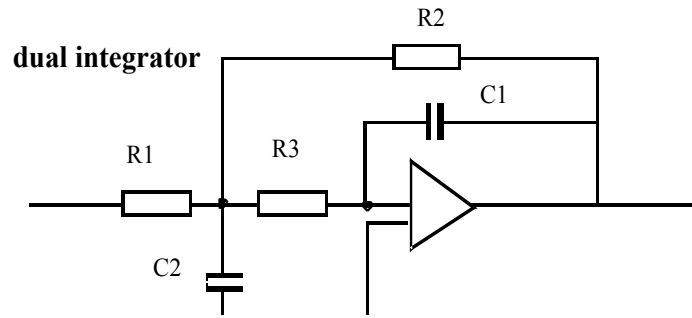


Fig. 10. Dual integrator circuit with multi-feedback architecture.

The dual integrator transfer function can be expressed [6] with gain K, as second order polynomial of the Laplace  $s$  operator :

$$H(s) = \frac{K}{1 + as + bs^2}$$

For a flat Bessel filter transfer characteristics of second order, the following conditions for the coefficients of the polynomial apply:

$$K = R_2/R_3 \quad (\text{gain of dual integrator for } f \ll f_c)$$

$$a = \omega_c C_1 (R_2 + R_3 + R_2 R_3 / R_1) = 1.3617$$

$$b = \omega_c^2 C_1 C_2 R_2 R_3 = 0.618$$

In order to avoid complex solutions the capacitor values must fulfil the condition:

$$C_2 \geq C_1 \frac{4b1K^2 - a^2}{a}$$

The solutions for the resistances, given a set of capacitor values and a shaper gain K for a cutoff frequency  $f_c = 1/(2\pi \tau_0)$  with shaping time constant  $\tau_0$ , are shown below:

$$R_1 = \frac{R_2}{-K}$$

$$R_3 = \frac{b}{4\tau_0^2 f_c^2 C_1 C_2 R_2}$$

The frequency scaling factor is  $FSF = 1.2736$ . The values obtained for 1 and 2  $\mu s$  shaping time and high gain are shown in Table 2.

$\tau_0$	R1	R2	R3	C1	C2	K
2 $\mu s$ (high gain)	649 $\Omega$	4.42 k $\Omega$	1.78 k $\Omega$	150 pF	2.2 nF	3.35
2 $\mu s$ (low gain)	10.5 k $\Omega$	4.22 k $\Omega$	5.90 k $\Omega$	220 pF	470 pF	0.21
1 $\mu s$ (high gain)	681 $\Omega$	4.87 k $\Omega$	1.96 k $\Omega$	68 pF	1000 pF	3.35
1 $\mu s$ (low gain)	4.02 k $\Omega$	1.69 k $\Omega$	5.36 k $\Omega$	150 pF	470 pF	0.21
100 ns (high gain)	78.7 $\Omega$	316 $\Omega$	205 $\Omega$	100 pF	1000 pF	1.95
100 ns (low gain)	590 $\Omega$	147 $\Omega$	442 $\Omega$	220 pF	470 pF	0.12

Table 2. CR-RC2 shaper component values for three shaping constants.

The full implementation of one dual shaper channel with high and low gain, including pole-zero-compensation is depicted in Fig. 11 for the 2  $\mu$ s shaping time. An anti-aliasing filter of ca. 4 MHz cutoff frequency has been added between the differential shaper output and the ADC.

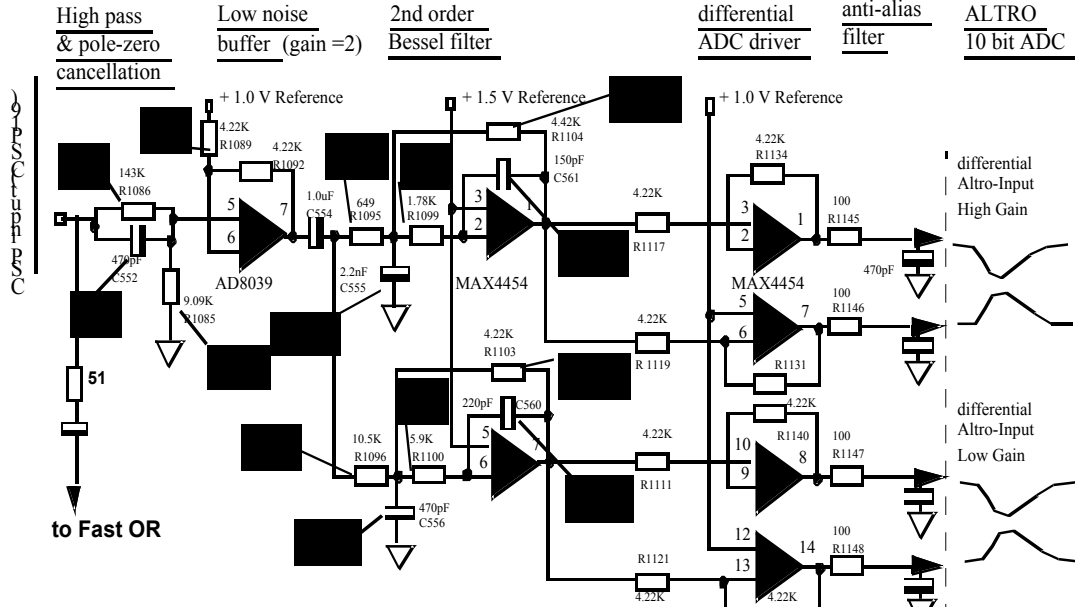


Fig.11. Detailed schematics of one dual-shaper channel for 2 $\mu$ s shaping time.

## Digitization and triggered readout

As shown in Fig. 4, the 20 dB cutoff frequency of the input signal after the shaper bandpass is around 600 kHz, i.e. the Nyquist frequency ( $2 \times$  signal bandwidth) is less than 2MHz, hence a sampling frequency  $f_s = 2$  MHz is sufficient. For the measurements presented below, over-sampling at 10 MHz is applied in order to study also sampling frequency dependence. The ADC is an ALTRO chip [7] containing multiple sampling buffers of up to 512 samples. The loading of the data buffer with ADC samples requires a timing strobe in order to start transfer of samples from a 15-deep pre-sampling pipeline into the data buffer. The timing strobe latency (derived from the trigger of the experiment) must therefore not arrive later than  $10/f_s \mu$ s after the signal, in order to store at least 5 pre-samples for measuring the pedestal and RMS noise. The digitized pulse-shapes are read out from the data buffers via the custom protocols of a custom 40 bit bus. The readout master for up to 28 FEE cards is a combination of a Readout Control Unit (RCU) [8] module and networked processor node (DCS) [9]. The protocols include remote access to all FEE registers which are defined by programmable slave logic (PCM) of the FEE cards. The data transfer from ALTRO data buffers to the offline computers is established via the custom, optical DDL link [10] of the ALICE experiment.

## Offline analysis

For offline data analysis, the Root analysis package [11] developed at CERN is used. Fig 12 depicts the Root reconstruction of a typical 2 GeV equivalent and pole-zero-compensated LED pulse. This example depicts the high-gain shaper with 1 $\mu$ s shaping time, sampled at 10 MHz. The Gamma-2 fit extends from the first pre-samples up to sample 60 (6  $\mu$ s). In the test environment, the strobe latency was set to 15 pre-samples, used to determine pedestals and RMS noise.

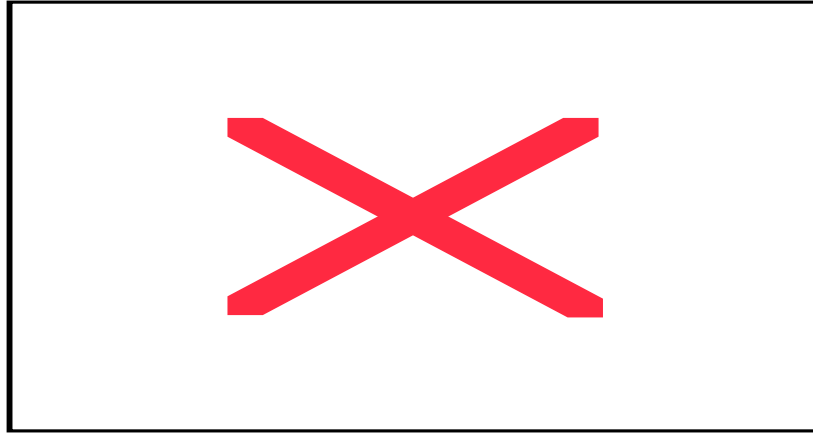


Fig. 12. Offline high gain ADC counts versus samples [100 ns]. The red area is a Gamma-2 fit.

After pedestal correction, the signal peak amplitude is 410 ADC counts and the peaking time corresponds to 2  $\mu$ s. Since the dynamic range definition implies that 5 MeV corresponds to 1 ADC count, the peak amplitude corresponds to 2.05 GeV.

## FEE prototype response to electrons

The first FEE card prototypes were tested with a triggered electron beam directed to a 16 by 16 PWO<sub>4</sub> crystal matrix [3] in August 2004, and with mixed beams of protons, pions, and electrons with momenta of 4 to 120 GeV/c directed to an 8 by 8 array of EMCal towers in November 2005. Fig. 13 shows the digitized pulse shape output with 10MHz sampling (100ns/channel) for an electron event in PHOS (Left) and a proton event in EMCal (Right). The different peaking times of 2  $\mu$ s and 200ns, respectively, corresponding to the different shaping times are apparent.

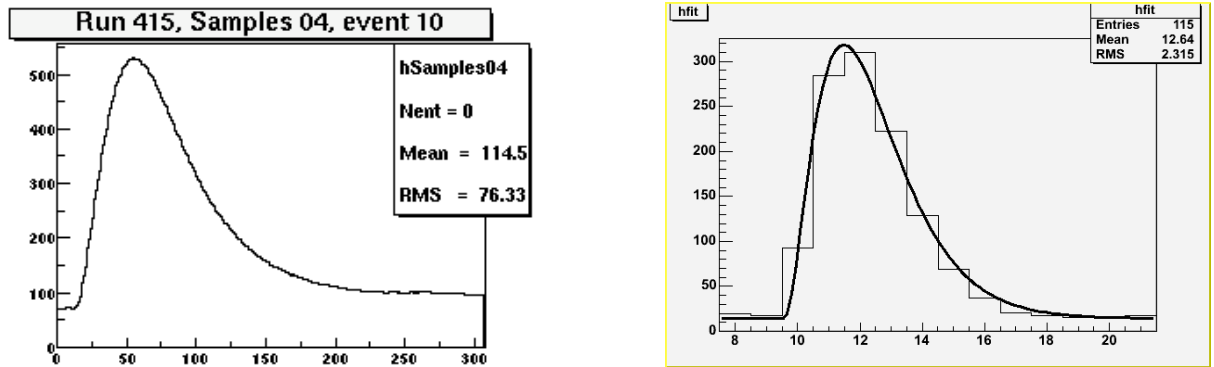


Fig. 13. FEE electronic pulse shapes (100ns/channel) with testbeam: Left-PHOS, Right-EMCal.

The test beam results confirm the FEE gains and shaping times and will allow to extract the light yields from the calibrations in terms of MeV/ADC count and to extract the overall energy resolution including the FEE noise contribution. Gain adjustments within a factor 2 are easily accomplished via APD bias adjustment. Later revised FEE cards have significantly less noise.

## FEE card

The architecture of FEE electronics within the PHOS readout and trigger system has been described in [12] and [13]. The photograph of Fig. 14 shows the 10 layer FEE card with all of its details. The total power consumption is 5 Watt.

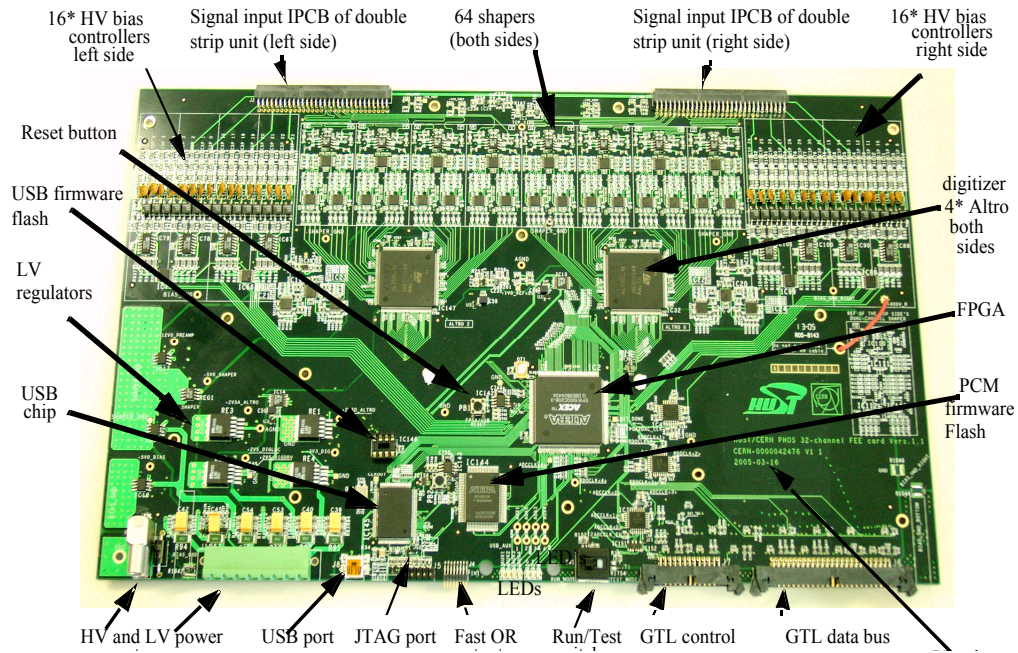


Fig. 14. Photograph of the 32 channel FEE card.

Special attention was given to a hierarchical power filtering and careful layout of ground planes for analogue, digital, and high voltage sections, avoiding coupling of digital noise into the analogue shaper sections. With temperature and current monitoring, individual FEE cards within a closed detector volume can be disabled in case of power or temperature problems. The cards are designed for operation inside water cooled copper cassettes. For this purpose, the FEE component layout leaves room for inlet and outlet water pipes and contains holes for mounting screws of the surrounding cassette.

## Test environment

A test environment with APD diodes requires ideally the same conditions as existent in the calorimeter, i.e. a stable ambient temperature of -25 C and a pulsed photon light source with similar wavelength and timing

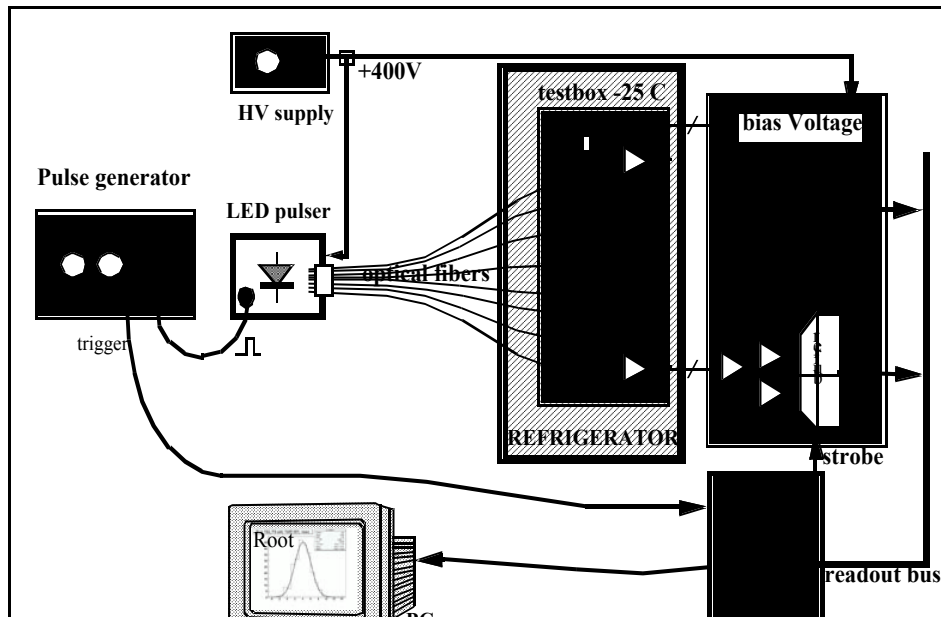


Fig.15. Test environment in the Wuhan PHOS laboratory at CCNU.

characteristics as scintillating light produced by electromagnetic showers in  $\text{PWO}_4$  crystals. The corresponding test setup of the PHOS laboratory in Wuhan is shown as a simplified diagram in Fig 15. The inputs of the FEE card are connected to an array of APD/CSA in a testbox which is kept inside a refrigerator at a temperature of  $-25^\circ\text{C}$ . A pulse generator is used to trigger an avalanche LED pulser, containing a LED with 470 nm peak spectral emission. The emitted light-pulse is distributed via optical fibers to the APD array. All APD's have been set via bias voltage registers to a gain value which generates the same amplitude for the common light input. Upon reception of the trigger output from the pulse generator, the Readout Control Unit (RCU) sends a timing strobe to all ALTRO chips to store ADC samples of all selected channels into their readout buffers. Thereafter, these buffers are transmitted, via the RCU and the optical fiber DDL link to a Data Acquisition Computer. The Root analysis tools are used to sort all sampled ADC data in histograms and to perform user defined data analysis. The results are shown and discussed in the following chapters.

## LED pulser

An avalanche LED pulser [14] was built for the test setup to generate up to  $10^8$  photons of 470 nm for distribution via optical fibers with a 1-2 ns light risetime. Fig 16 shows the 13 Volt pulse amplitude of 2 ns risetime and the APD testbox with optical fibers.

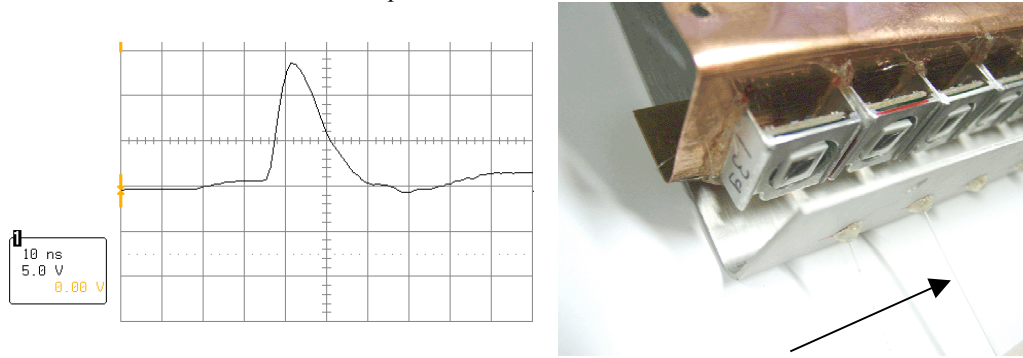
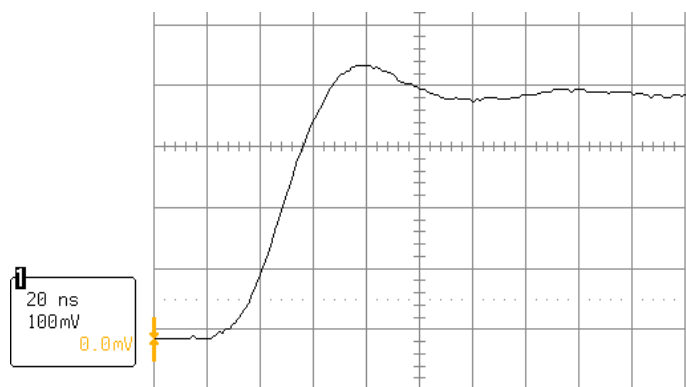


Fig. 16. Left: Pulse at the pins of a Kingbright L7104PCB / Right: APD test box with optical fiber input.

The charge/voltage step response of the CSA, which corresponds to a photon flash from a pulse like Fig 16, transmitted over ca. 50 cm of optical fiber to the APDs, is depicted in Fig. 17. The LED (Kingbright L7104PCB) is specified for typically 350 milli-candela @ 20 mA. When measured over a series resistor, the pulse corresponds to 0.7A peak current, which can be converted over lumen and human eye correction factors into  $8 \cdot 10^8$  photons.



The step function of the attenuated light flash, measured in this test by APD and CSA, shows a slight overshoot which is due to the test-setup and due to crosstalk from the pulser. This effect is not observed with real particles in the testbeam.

Fig.17. CSA output response to a LED pulse.

## Fast analog OR

A threshold trigger can be based on individual analog sums from  $2 \times 2$  input channels. A trigger region unit (TRU) was designed [15] to receive all fast OR signals from 14 FEE cards and to generate charge sums over  $4 \times 4$  sliding windows. In order to generate an analogue sum from 4 input channels, the input signals on the FEE cards are split (compare Fig. 11) into semi-gaussian energy channels and into fast-OR trigger channels with 12-bit dynamic range. The fast OR's are generated by simple RC shaper with 100 ns pulse width.

## Measured FEE characteristics (1 $\mu$ s shaping time)

The measurements presented here are results of the Root offline analysis with data generated via the test system and read out via a computer for offline analysis.

### Linearity and gain over dynamic range

The theoretically linear relation between the peak amplitude of the Gamma-2 function and the APD charge (input voltage step amplitude) was confirmed by the measurements of Fig. 18.

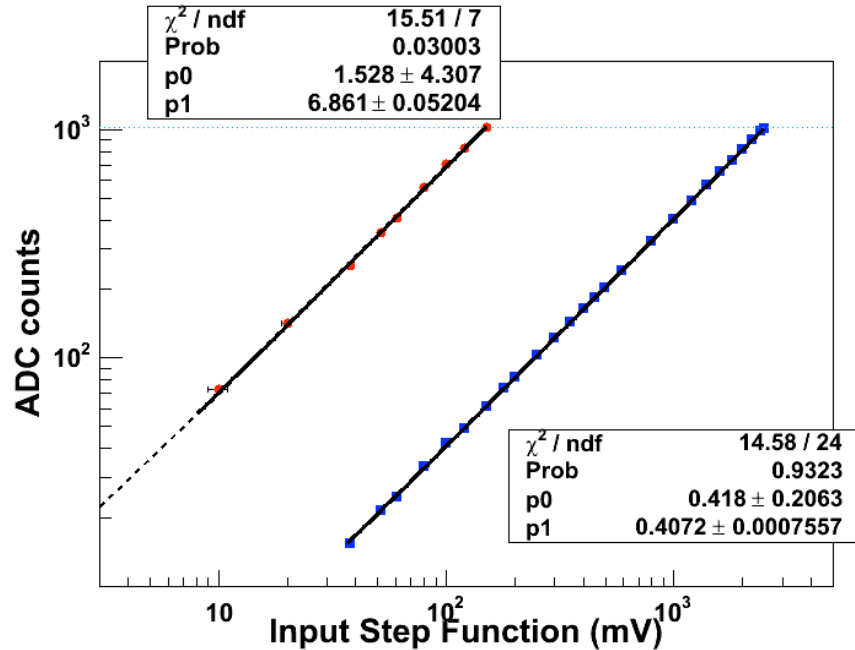


Fig. 18. Linearity measurement over dynamic range.

The lower curve represents the full low gain range (2.3 mV...2.39 V input step ) the upper line shows the high gain range up to 0.149 Volt. The measurement had to be extrapolated towards input step voltages below 10 mV since step voltage levels from 146  $\mu$ V to 10 mV could not be measured precisely with external instruments.

The two shaper gains can be derived from the slope values (p1 coefficient) after converting ADC counts in Voltage according to 1ADC bit = 1V/1024=0.9765 mV. With this,

- Low gain, measured = **0.4072 +- 0.001**
- High gain, measured = **6.861 +- 0.052**

These values correspond with the values defined in chapter “Dynamic Range”.

### APD gain calibration

The gain spread of the APDs for a given bias voltage was measured in a PHOS testbeam October 2004 with the first FEE prototypes with 2 GeV electrons and with an overall bias voltage of 340 Volt. Fig 19 shows the gain distribution before and after FEE gain calibration after individual bias adjustment via bias registers. The uncalibrated variations amount to more than 300%. After (non-exhaustive) hardware calibration the variation is shown to be reduced to ca. 5%.

Individual gain control via 10-bit bias voltage registers on the FEE cards allows for controlled gain calibration of 0.16Volt per bit in the range 240-400Volt. With  $1/M \times (dM/dV) = 3.3\%$  for gain  $M=50$  [21] and a bias voltage granularity of 0.16Volt, the gain resolution (for constant temperature) is 0.48%.

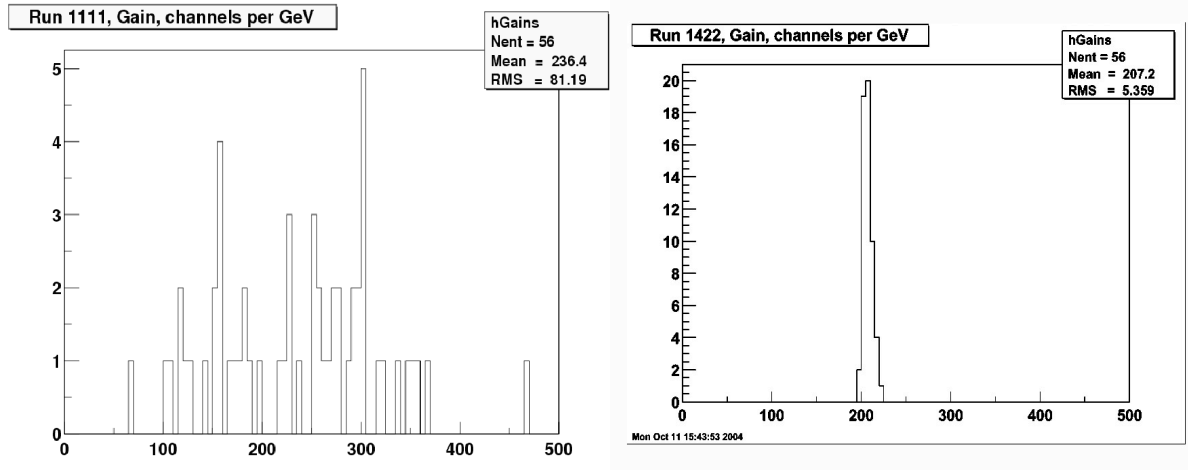
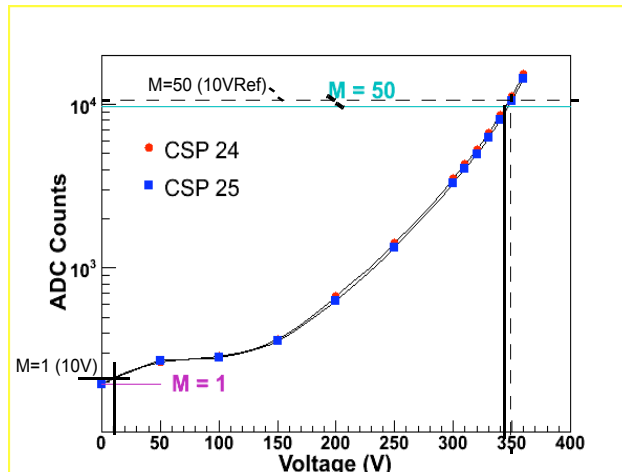


Fig. 19. APD gain spread at -25 C with 2 GeV particles (left). APD gains after hardware pre-calibration (right).

The determination of the bias voltage-gain correspondence of individual photodiodes requires knowledge of their signal amplitude for gain  $M=1$ . By measuring the signal amplitude at gain  $M=1$ , and amplified by the desired gain, one obtains the corresponding bias voltage. Such a measurement is shown in Fig. 20 over the full bias voltage range for two APD's.



This determination of the gain  $M=1$  is not very precise and depends also on the light wavelength. As described in [16], APD gain 1 should be measured at a bias Voltage of 10 Volt due to the large increase of diode capacitance at low voltages. With this, the nominal gain of  $M=50$  at -25C is reached at ca. 350 Volt for the two APD's.

Fig. 20. APD gain curve for two APDs at -25 C. Gain 50 is reached at around 350 Volt if gain  $M=1$  is determined at 10 Volt.

In view that an inter-calibration of less than 1% is aimed for in the noise term of the energy resolution, this method of gain calibration is only useful for pre-calibration, while inter-calibration to the 1% level requires calibration with cosmic or testbeam particles.

## Pedestal and RMS measurement

The pedestal and RMS measurements are taken from the pre-samples of the digitized signal as shown in Fig. 10, by measuring over  $N$  triggered events.

For an unconnected FEE card, Fig 21 shows the Root evaluation of pedestal distribution over all 32 high gain FEE shaper channels (bottom) and their derived RMS noise (top) for 2050 events. The variation of pedestal levels is normal due to component tolerances. The uniform RMS noise level around 0.25 ADC counts corresponds closely to the ADC quantization error.

After connecting 8 APD detectors in an absolute dark environment with gain setting  $M=50$  and at -25° C to the FEE channels 24...31, the noise distribution is a little more disturbed as shown in Fig 22. There is however a clear RMS enhancement of the APD channels over the unconnected channels to an average 0.262

ADC counts. With the dynamic range definition of PHOS, 1 ADC counts corresponds to 5MeV, hence the RMS noise is 1.31 MeV. Note that the pedestals are unchanged.

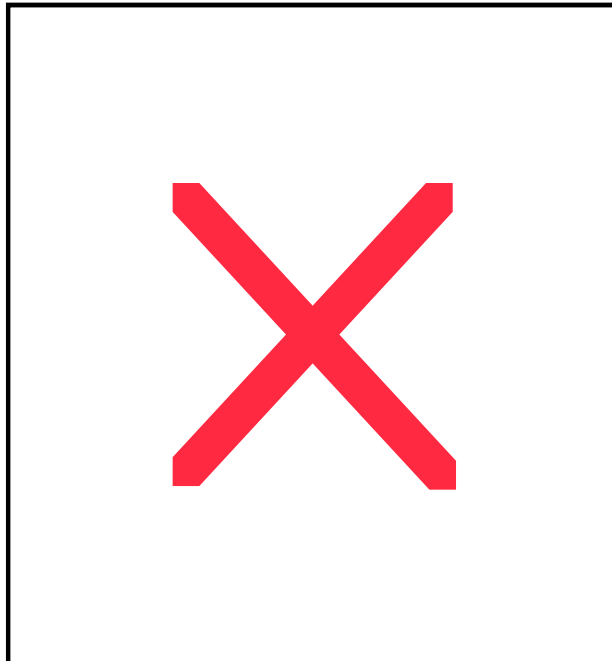


Fig. 21. Pedestal and RMS noise measurement for a FEE card without detector connected.

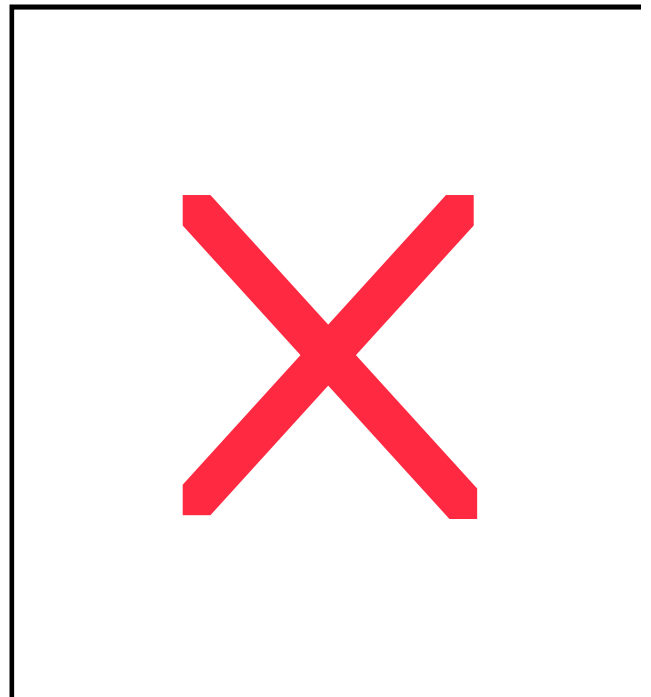


Fig. 22. Pedestal and RMS noise measurement with 8 APD's connected and 24 channels unconnected to a FEE card.

The pedestal and RMS noise plots for the high gain channels are not shown here.

## APD noise as function of bias voltage

As shown in section “signal over noise” the serial noise dominates at shaping times below the minimum noise, hence the APD current has little influence at shaping times below  $2\mu\text{s}$ . However the APD capacitance is a strong function of the bias voltage with a strong increase of capacitance (noise) towards low voltages. Towards higher bias voltages, the excess noise, due to charge avalanche, increases the effective noise level. Fig. 23 depicts a measurement of the all inclusive noise versus bias voltage. Though only 8 APDs were used, the effect of excess noise can be seen above 360 Volt. The average noise at gain 350 Volt ( $M=50$ ) is less than 0.3 ADC counts (1.5 MeV). At higher gain settings, some APD's start showing excessive noise.



The excess noise is a statistical process which broadens the signal resolution, hence belongs to the stochastic term “b” of the spectrometer’s energy resolution. Given an excess noise factor of F=2.27 for gain M=50 it can be shown that [16]

$$\frac{b}{\sqrt{E}} = \sqrt{\frac{F}{N_{pe}}}$$

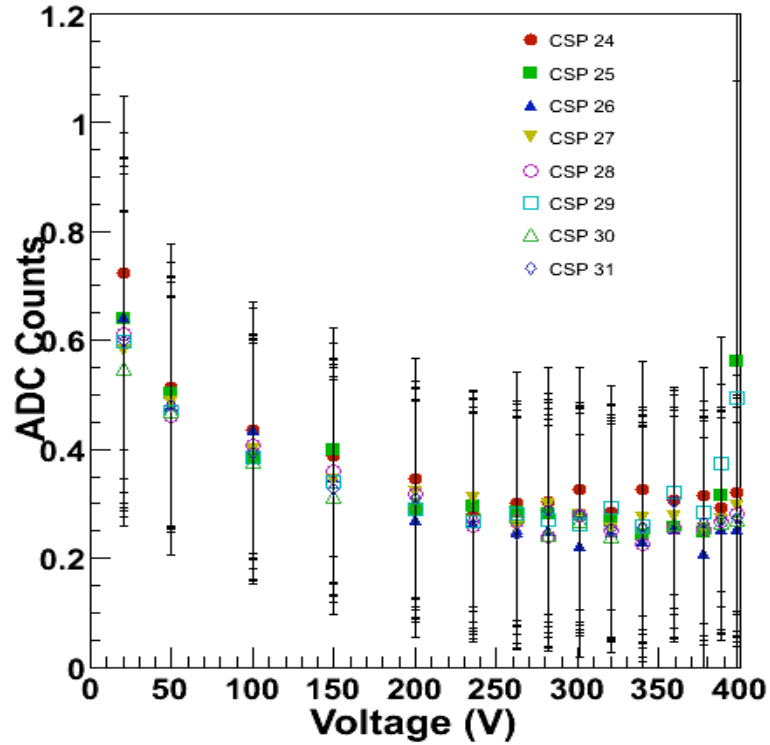
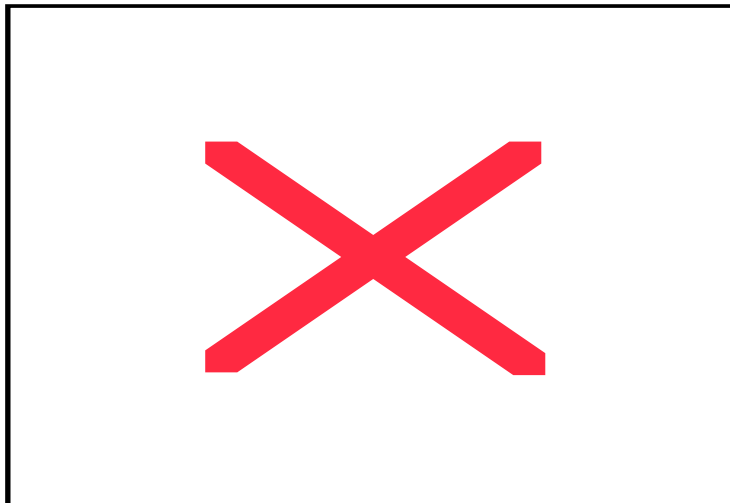


Fig.23. Measurement of effective noise (ADC counts) versus APD bias voltage for 8 APDs on FEE electronics.

With  $N_{pe} = 4 \text{ e- / MeV}$  and  $F=2.27 @ (M=50)$ , the lower limit of the single channel stochastic term at 1 GeV can be approximated as  $b > 2.3 \text{ \% GeV}$ .

## Gain ratio of high:low gain

The design gain ratio for FEE cards (high gain:low gain= 16:1) of the two shapers sections cannot be implemented exactly as 16:1. The 32-channel gain ratio measurement of Fig. 24 reports a value of 16.83 which effectively increases the dynamic range to 14.075 bits.



This measurement also demonstrates excellent uniformity achieved with discrete component shapers on the FEE cards.

Fig. 24. Uniformity of gain ratio High/Low gain.

## Peaking time measurement

The design peaking time of the second order FEE shapers with  $1\mu\text{s}$  shaping time is  $2\tau = 2\mu\text{s}$ . Fig. 25 shows the Root measurement taken with 8 APD's pulsed by a LED flash for obtaining a peaking time distribution. The measured mean value is  $2.175 \pm 0.01\mu\text{s}$ .

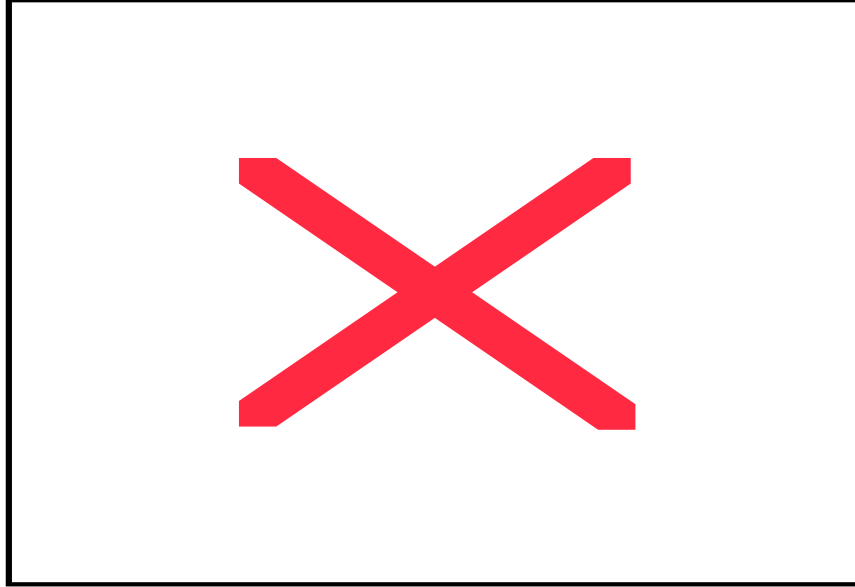


Fig. 25. Peaking time measurement of the FEE shaper with  $1\mu\text{s}$  shaping time.

## Timing resolution

Great attention was given to the PHOS requirement of a timing resolution of the order 1 to 2ns, for time-of-flight cuts that will be used to discriminate against anti-neutron background, predominantly around 2 GeV. The timing resolution achievable with semi-gaussian shapers is a weak function of noise and shaping time but a strong function of the signal amplitude (ADC bits) and of the sampling frequency. Considerable improvement was however gained by using the proper offline method and by using a LED pulser with light risetime of the same order or better than the targeted resolution.

The intrinsic timing resolution of  $\text{PWO}_4$  crystals is 0.13ns [14] and absolute time measurements with precision time-digital converters have achieved a constant timing resolution of 0.5 ns above 1.5 GeV. The only affordable way of measuring time-of-flight in each individual channel is by offline determination of the time reference from the Gamma-2 fit. In order to achieve this level of timing resolution, it is important to first determine the peaking time of each individual channel and then use these values for Gamma-2 fits.

### Timing resolution of FEE card

The method applied for measuring the differential timing resolution of the FEE alone is depicted in Fig 26. A step voltage of equivalent energy E is connected to the inputs of two or more shapers. The differences of the time references  $t_1$  and  $t_2$  of the offline fits are compared and the differences are accumulated in a histogram.

With significantly high statistics, the variance of the difference plot  $\sigma(t_2 - t_1)$  is a measure of the differential timing resolution. Assuming both channels have the same resolution, the timing resolution is  $\sigma/\text{SQRT}(2)$ .

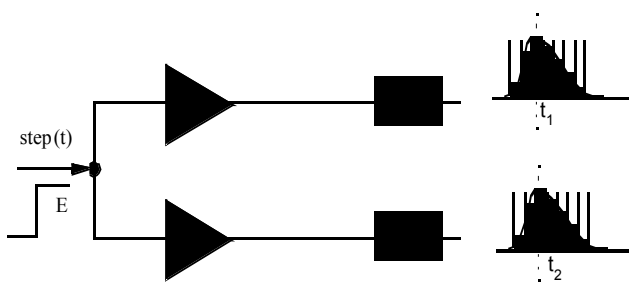


Fig. 26. Principle of measuring differential time resolution measurement.

The measurement of the differential time resolution of 2 FEE channels without detector, using only a step pulser of 2 GeV equivalent energy is shown in Fig 27. With 2050 events and a sigma of 0.712, the differential time resolution of PHOS FEE electronics at 2 GeV is 0.5 ns.

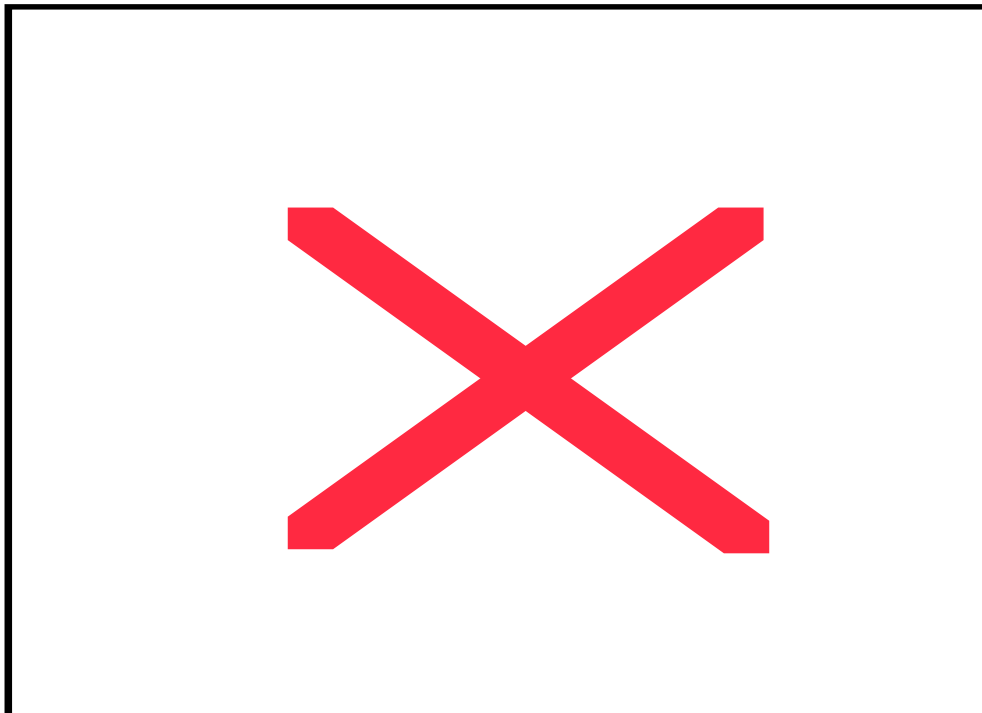


Fig. 27. Offline measurement timing resolution of pulsed FEE channels.

A strong energy dependence of the offline timing resolution measurement is shown in Fig. 28. It is due to the digital resolution limit of the dynamic range, as shown in Fig.1. In the limit of 10 bits (1024 counts) signals, the FEE electronics can resolve 300 ps at a shaping time of 1  $\mu$ s. This result hints that for future upgrades, the digital resolution should be increased to a dynamic range of 16-bit.

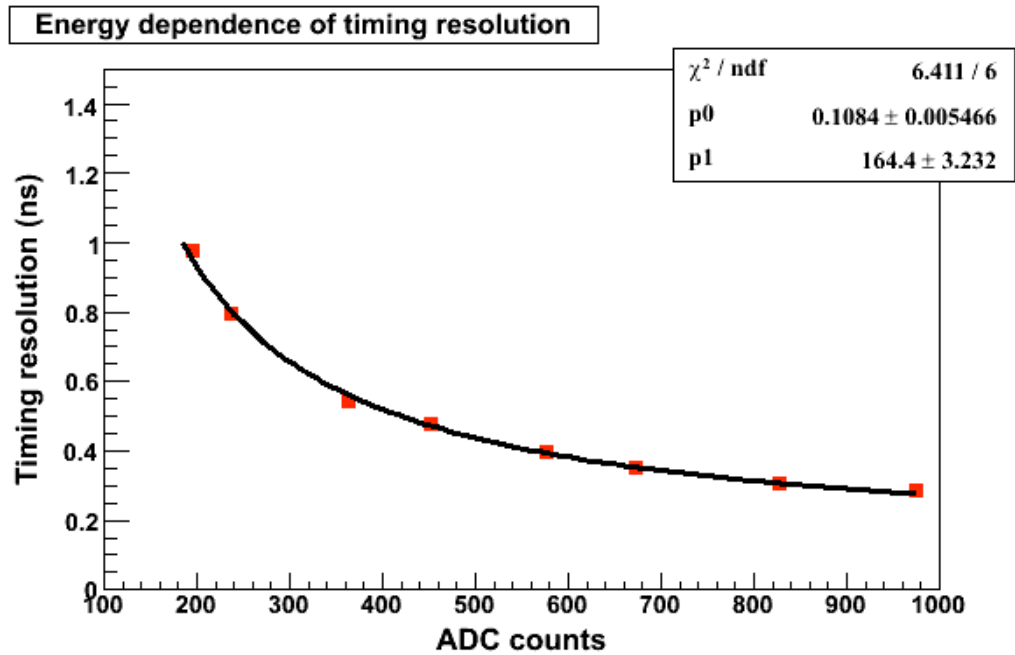


Fig. 28. Timing resolution dependence on equivalent energy (ADC counts).

## Timing resolution with APD and LED source

The timing resolution with particles and APD's can be measured in good approximation by placing the APD's within the same bias, temperature, and connectivity environment as in the experiment and by pulsing a LED of similar wavelength and timing characteristics as scintillating light of the  $\text{PWO}_4$  detector. The test environment described previously provides this possibility. The timing resolution measurement is depicted in Fig 29 (high gain) and Fig 29 (low gain). The equivalent LED light energy was ca. 2 GeV (compare Fig 11 for amplitude of the pulses of Run 157).

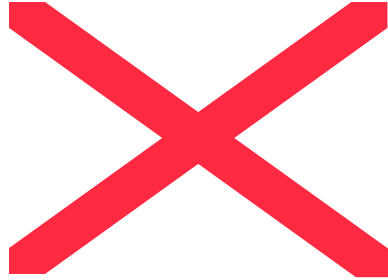


Fig. 29. High gain timing resolution at 2 GeV with LED.

The differential time resolution of the high gain section is 1.5 ns and of the low gain section 6.22 ns. The combined high/low timing resolution for 1  $\mu\text{s}$  shaping time at 2 GeV equivalent energy is:

$$\tau_{\text{res}} (1\mu\text{s}) = 1.455 \pm 0.026 \text{ ns}$$

The difference in resolution with and without APD/preamplifier of ca. 1 ns is due to the limited timing resolution of the APD (order 400 ps) and finite risetime of the LED light.

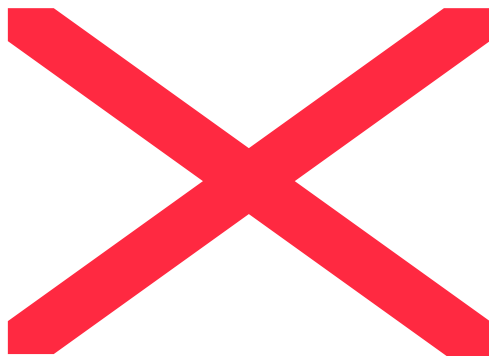


Fig. 30. Same timing resolution as in Fig 29 but measured in the low-gain channel. The resolution is worse compared to the high gain channel due to the lower digital resolution at 2 GeV.

## Timing resolution dependence on sampling frequency

The timing resolution obtained with a LED source is shown in Fig. 31 as a function of ADC sampling frequency. The plateau above 1 MHz sampling frequency complies with the Nyquist theorem that a sampled signal is fully defined by sampling it at twice the signal bandwidth. As shown in Fig.4, the -20db signal bandwidth above  $f_c$  is ca 600 kHz for 1  $\mu$ s shaping time. With 10 MHz sampling rate, semi-gaussian signals for 1  $\mu$ s shaping time are by far over-sampled. Unless over-sampling [18] methods can be used offline to

improve timing resolution (via gaining more effective bits), a sampling frequency of 2 MHz is sufficient for 1  $\mu$ s shaping time.

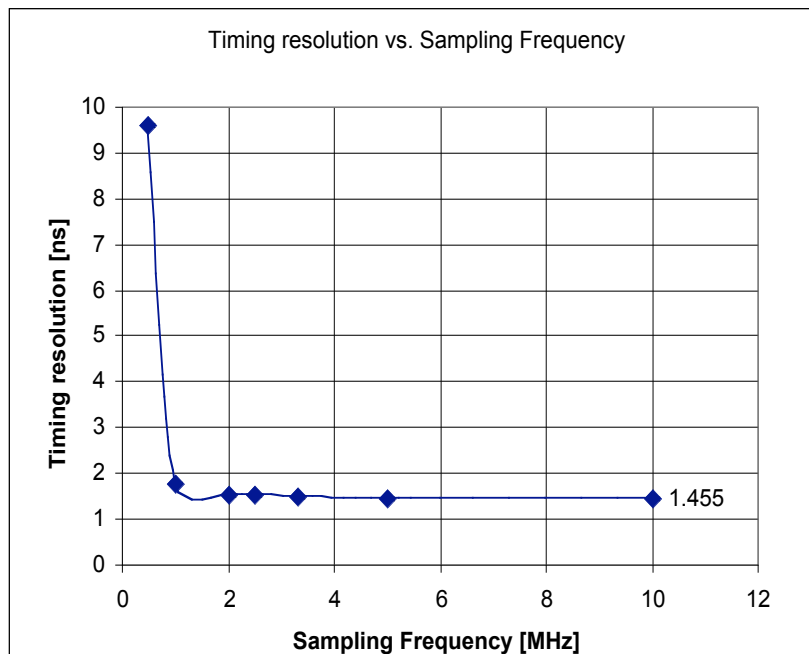


Fig. 31. Measurement of timing resolution dependence on the ADC sampling frequency.

## Comparative measurement with 2 $\mu$ s shaping time

As depicted in Fig. 6, a shaping time of 2-3  $\mu$ s should result in even lower RMS noise. Fig. 32 confirms this for 2 $\mu$ s shaping time by a measurement under exactly the same conditions as Fig. 22. Obviously the ENC noise from the shaper reaches the noise limit of the ADC at 0.221 ADC counts.

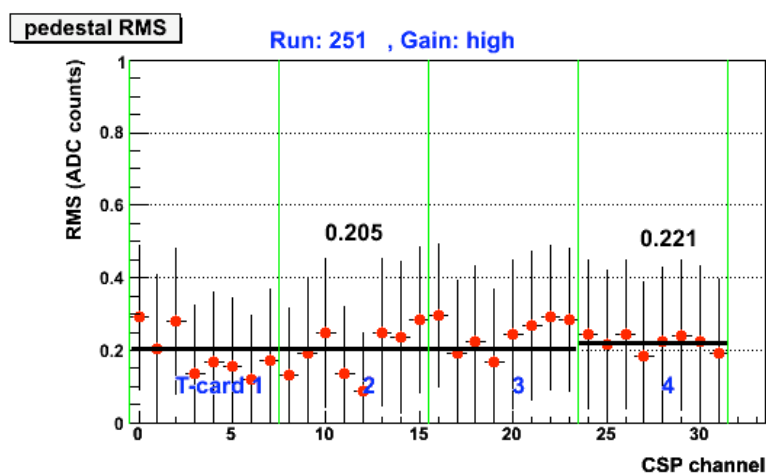


Fig. 32. Comparative measurement of Fig. 22 but with 2  $\mu$ s shaping time.

The reduced noise with 2  $\mu$ s shaping time is opposed by a reduced timing resolution of 1.76 ns as measured in Fig. 33 with a LED source under the same conditions as Fig 29. A conclusion from the two comparative measurements is that the ca. 18% RMS noise reduction has less importance for PHOS than the ca. 17 % improved timing resolution, and therefore a 1  $\mu$ s shaping time has been adopted.

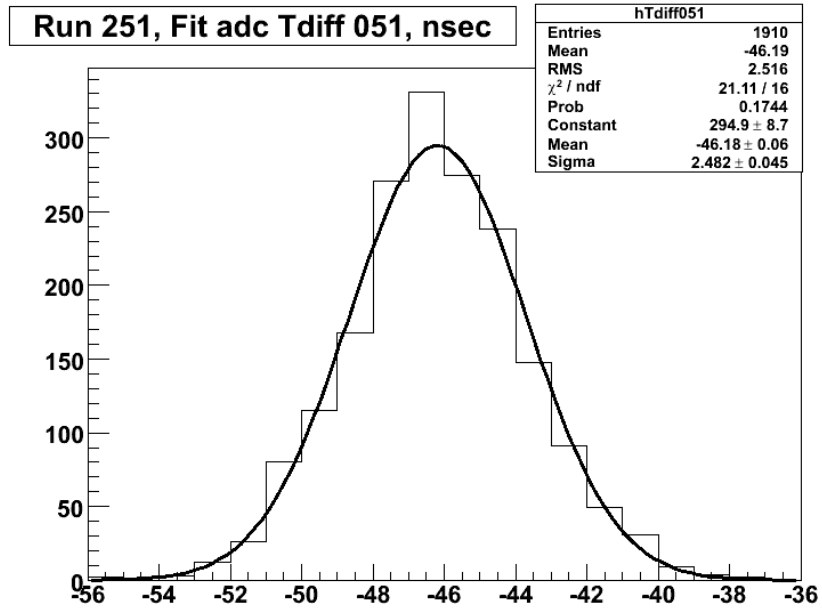


Fig.32. Comparative measurement of Fig. 28 with 2 $\mu$ s shaping time.

## Conclusions and Outlook

The 32-channel low noise FEE electronics presented here has been designed for the high resolution PHOS electromagnetic calorimeter for a dynamic range of 14-bit. The design performance goals for the PHOS calorimeter have been verified by measurements in the dedicated test facilities at CCNU and HUST in Wuhan, China. With cooled APD's and a shaping time of 1 $\mu$ s, the noise level at an APD gain of 50 is less than 10 photoelectrons (0.26 ADC counts) and the offline timing resolution is better than 1.5 ns. The configurable shaper properties and the hardware gain calibration feature allow for adaptation to other photon detectors. The EmCal project of ALICE [19] has adopted this electronics with 100 ns shaping time. An upgrade towards 16-bit dynamic range for better timing and noise performance and a direct, optical readout concept [20] between FEE and PC via 1 Gbit/s network protocols is under consideration.

## Acknowledgements

This work is supported by the Alice LHC project at CERN, by the Norwegian Research Council and INTAS Project 03-5747, by the Natural Science Foundation (NSCF) of China and the China Ministry of Education (CMOE) under Grant reference 10575044, 10547118, (2005) 0360731 and sponsored by SRF for ROCS, SEM, by Central China Normal University (CCNU) under grant reference (2005)80 and by the US Department of Energy under contract no. DE-AC05-00OR22725.

## References

- [1] Photon Spectrometer PHOS, ALICE Technical Design Report, CERN /LHCC 99-4, 5 1999
- [2] A high resolution electromagnetic calorimeter based on lead-tungstate crystals, D.V.Aleksandrov et al., Nucl. Instr. and Methods in Physics Research A, Vol. 550 Issues 1-2 (2005), pp 169-184
- [3] Energy, Timing and Two Photon Invariant Mass Resolution of a 256 channel PWO Calorimeter, M. Ippolitov et al., Proceedings CALOR 04 Conference April 2004, Perugia, Italy
- [4] Review of Particle Physics, Vol. 15 No1-4 (2000) Chap. 24.9 Particle detectors, Low Noise Electronics
- [5] Limits of Low Noise Performance of Detector Readout Front Ends in CMOS Technology, W.M.C Sansen et al. IEEE Trans on Circuits and Systems, Vol. 37 No 11, Nov. 1990

- [6] Active Filter design techniques, Chapter 16, Texas Instruments, Literature Number SLOD006A ( Excerpt from “O-Amps for Everyone”)
- [7] The Altro chip: A 16-channel A/D converter and digital processor for gas detectors, Proc. IEEE NSS/MIC , November 2002, Norfolk
- [8] The Readout Control Unit of the ALICE TPC, Thesis, Lien, J.A. CERN-THESIS-2005-013
- [9] Front-End-Electronics Communication software for multiple detectors in the ALICE experiment, S.Bablok et al. submitted to Nucl. Instr and Methods A, 2005
- [10] The ALICE Detector Data Link, György Rubin et al. Article p493 in CERN report 99-9
- [11] ROOT, An Object-Oriented Data Analysis Framework, <http://root.cern.ch>
- [12] Front-End Electronics for PWO-based PHOS Calorimeter of ALICE, H.Muller et al. Proceedings Fourth International Conference on ‘New developments in photodetection’ Beaune, France, 19-24 June 2005, submitted to NIM-A
- [13] Trigger electronics for the Alice PHOS detector, Nucl. Instr. and Methods in Physics Research, A Vol 518 (2004), pp 525-528
- [14] LED calibration system of the lake Baikal neutrino telescope NT-200+, B.K. Lubsandorzhiev et al. 29th International Cosmic Ray Conference Pune (2005) **00**, 101-104
- [15] Trigger Region Unit for Alice PHOS Calorimeter, Proceedings LECC05, 11<sup>th</sup> Workshop on Electronics for LHC and future Experiments, Heidelberg, September 2005
- [16] Characterization of avalanche photodiodes for calorimetry applications, A. Karar et al. NIM A ,428(1999), Issues 2-3, 413-431
- [17] Response of a PbWO<sub>4</sub> scintillator array to electrons in the energy regime below 1 GeV, R.Novotny et al., IEEE TRANS. Vol. 44, issue 3, Part 1, (1997) 477-483
- [18] Oversampling Methods for Data Conversion, J.C. Candy, G.C.Temes, IEEE Pacific Rim Conference on Communications, Computers and Signal Processing, May 9-10, 1991
- [19] EMCAL ALICE-USA DOE report on Electronics [http://rhic23.physics.wayne.edu/twiki/pub/Alice/ReviewDocs/Readout Technical Summary](http://rhic23.physics.wayne.edu/twiki/pub/Alice/ReviewDocs/ReadoutTechnicalSummary)
- [20] Common Gigabit interfaces for HLT and L1T trigger links of LHCb, H.Muller et al. Proc. 9<sup>th</sup> Workshop on Electronics for LHC, Amsterdam, Sept 29-Oct.3 2003, Report CERN LECC-2003-055, p139 ff.
- [21] Investigation of Photon Detection Efficiency for Avalanche Photodiode (APD) Structure, F.Helvaci and I.Tapan, 5<sup>th</sup> General Conference of the Balkan Physics Union, Aug 25-29, 2003, Vrnjacka Banja, Serbia and Montenegro

Corresponding Author: Hans Muller, CERN PH, CH-1211 Geneva 23, Switzerland, email: [Hans.Muller@cern.ch](mailto:Hans.Muller@cern.ch) Tel: +41 22 767 3533